Nanoscale

PAPER

View Article Online
View Journal | View Issue

Cite this: *Nanoscale*, 2015, **7**, 18179

Fano-resonant aluminum and gold nanostructures created with a tunable, up-scalable process†

F. Lütolf,[a,b] O. J. F. Martin[b] and B. Gallinet*[a]

Received 6th August 2015,
Accepted 1st October 2015

DOI: 10.1039/c5nr05316a

www.rsc.org/nanoscale

An up-scalable approach for creating Fano-resonant nanostructures on large surfaces at visible wavelengths is demonstrated. The use of processes suitable for high throughput fabrication and the choice of aluminum as a cost-efficient plasmonic material ensure that the presented insights are valuable even in consideration of typical industrial constraints. In particular, wafer-scale fabrication and the process compatibility with roll-to-roll embossing are demonstrated. It is shown that through adjustment of readily accessible evaporation parameters, the shape and position of the optical resonance can be tuned within a spectral band of more than 70 nm. The experimental data are complemented with rigorous coupled wave analysis and surface integral equation simulations. Calculated electric fields as well as surface charges shed light onto the physics behind the present resonances. In particular, a surface plasmon polariton is found to couple to a localized plasmonic mode with a hexapolar charge distribution, leading to a Fano-like resonance. Further understanding of the interactions at hand is gained by considering both aluminum and gold nanostructures.

1 Introduction

The research field of plasmonics has received a lot of attention since the demonstration of extraordinary optical transmission (EOT) by Ebbesen *et al.*[1] Such Plasmonic resonances are capable of concentrating light to subwavelength volumes. This strong local field enhancement is of tremendous interest for many applications including sensing[2–4] and energy harvesting.[5] Plasmonic resonances are also found in optical security[6,7] or nano printing[8,9] since they can be spectrally controlled by adjusting fabrication parameters. This property, which we will in the following refer to as "tunability", can be utilized to generate a variety of strong colors and hence create entire images. It has recently been shown that such resonances can further be engineered in complex metallic systems making use of the Fano interference effect.[10] Fano-resonances occur when a radiative plasmonic mode couples to a non-radiative mode[11] or even two radiative resonances hybridize and form a combination of a superradiant and a subradiant mode.[12,13] The resulting spectrum then shows an asymmetric, narrow line shape, which is particularly favorable for sensing[14] and optical switching[15] since small spectral shifts lead to strong responses. Fano-resonances have been found in many different systems, ranging from split-ring[16,17] or dolmen structures,[18] over few-particle clusters,[19] to gratings.[10,20,21] Most of these structures however are expensive to produce for visible wavelengths on sizable areas, since they require serial patterning such as electron beam writing and ion beam milling.[22]

A particular class of nanowires having the shape of a split-ring resonator (referred to as U-shape in the following) can be generated using oblique deposition at both sides of a periodic nanostructure.[23,24] In the past decade, such nanowires have been used for investigating EOT effects in gold gratings[25] or for Surface Enhanced Raman Scattering (SERS).[26] Several theoretical studies have also investigated the role of Wood-Rayleigh anomalies (WR anomalies), or of various surface plasmon polaritons (SPPs), or groove modes in the optical response of U-shaped wires.[27–30] Although the oblique deposition process lends itself to low-cost, high-throughput production processes like roll-to-roll manufacturing,[31,32] past findings always relied on the use of noble metals and were limited to small areas since they included either electron beam patterning,[25] particle self-assembly[33] or extreme ultraviolet interference lithography to our knowledge.[34] As a matter of fact, gold and silver, both of which are expensive, are the most used materials in plasmonic nanostructures. This makes most of the reported structures unattractive for mass production.[35] Aluminum as a cost efficient alternative to the traditionally used noble metals has however recently received a lot of attention.[36] Besides its lower price, aluminum also has similar optical properties to silver at visible wavelengths,

[a]*CSEM Muttenz, Tramstrasse 99, Muttenz, 4132, Switzerland. E-mail: benjamin.gallinet@csem.ch*
[b]*Nanophotonics and Metrology Laboratory (NAM), Swiss Federal Institute of Technology Lausanne (EPFL), Station 11, Lausanne, 1015, Switzerland*
† Electronic supplementary information (ESI) available. See DOI: 10.1039/c5nr05316a

allows plasmonic resonances in the UV region of the spectrum (which could *e.g.* be interesting for fluorescence enhancement, energy harvesting or photocatalysis[35]) and is compatible with CMOS technology.[37] Aluminum structures also acquire a native oxide barrier layer which prevents further oxidation of the material.[38] The typical resonance broadening observed in aluminum at visible wavelengths when compared to identical noble metal structures can also become an advantage rather than a drawback, since color effects become less sensitive to fabrication imperfections.[8]

In this article, we present an up-scalable, low-cost process for the fabrication of Fano-resonant nanostructures based on nanoimprinting and oblique evaporation of metal. Aluminum and gold U-shaped nanowires are fabricated at wafer scale and show a variety of structural colors. Note that the laser interference lithography process used for origination of embossing masters can pattern a m^2 sized area[39] and the replication as well as evaporation processes employed are eligible for roll-to-roll production. Gold wires are considered first for their well-known optical properties. The use of computed near-fields, together with charge maps, elucidate the interaction mechanisms of the resonances at hand. We then transition to aluminum and make use of the main differences between the materials to elucidate the dynamics between the modes. We investigate in details near-fields and charges to corroborate our findings. Production line compatible ways for tuning the resonance position and shape on the fly are presented experimentally and compared to theory. We finally demonstrate the applicability of these structures for large-area color effects and sensing.

2 Results and discussion

The fabrication process is based on electroplating of nickel shims[40] from holographically originated masters and using them for replication *via* hot embossing[41] and UV casting[42] (Fig. 1(a)). These procedures, together with injection molding,[43,44] are standard in the industry. Although the more commonly used approach of writing individual structures in an e-beam lithography process has the advantage of being extremely versatile, it comes at the cost of a very slow patterning speed and is limited to small sample sizes. Stitching such small pieces together is also not yet possible without accepting clearly visible seams. The use of laser interference lithography allows us to pattern periodic gratings on a wafer scale[45] (up to m^2 sized nanostructures are commercially available[39]) and therefore circumvents these limitations of e-beam patterned or ion-beam milled replication masters.[46] Once the grating has been fabricated, the plasmonic resonances can still be tuned, even for fixed grating parameters. To this end, we use oblique metal deposition, which is a simple yet powerful technique for the fabrication of periodic, disconnected metallic nanostructures.[34] A binary grating of 350 nm period, 200 nm depth and w = 0.3 (see Fig. 1(d)) is used for all experiments. We evaporate aluminum or gold from both sides of the grating at the same angle α (Fig. 1(b)) to form U-shaped wires (SEM image, Fig. 1(c)). The structure is subsequently embedded in a polymer matrix to protect it from wear. This also simplifies the investigated resonant system, since the refractive indices of the substrate and the superstrate are matched. It is finally worth mentioning that the entire process is very well suited for high-throughput processes such as roll-to-roll manufacturing.

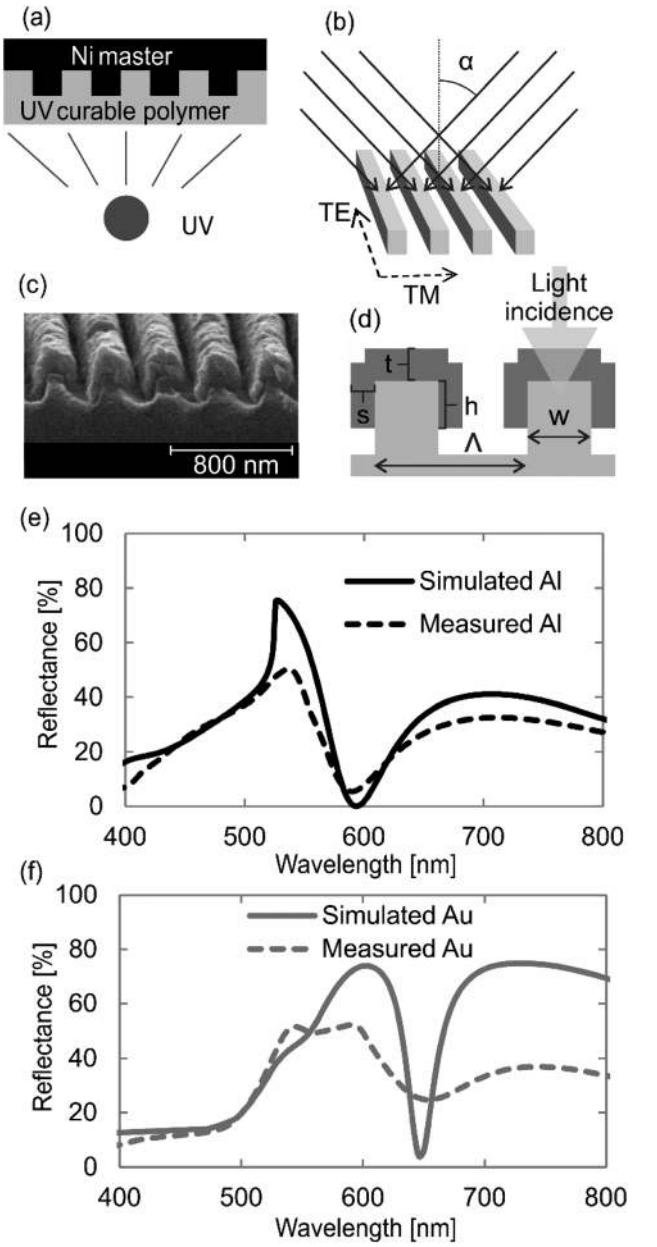

Fig. 1 The fabrication procedure consisting of (a) UV embossing and (b) double evaporation of metal at an angle α is shown together with (c) a SEM picture of the resulting nanostructures (aluminum) and (d) the corresponding model used for RCWA simulations. The resulting, measured spectra for TM polarized light are plotted for (e) aluminum and (f) gold, together with the according computations.

In order to obtain a Fano shaped resonance, at least one superradiant ("bright") mode has to be combined with one subradiant ("dark") mode. The former can for example be a

radiative plasmonic resonance such as an oscillating dipole. The latter needs to have non-radiative properties, which motivates resonators supporting quadrupolar charge distributions as popular choices. As recently described by Lovera *et al.*,[12] both of these modes can also occur when two bright resonances are hybridized. Typically, dipolar in-plane modes are utilized for this purpose since they are obtained in rod or disk shaped structures. Here, our modes of choice are a propagating surface plasmon polariton (SPP) and a localized plasmonic mode. The SPP is excited on the top surface of the metal grating (horizontal SPP, light incidence from the flat part of the U as indicated in Fig. 1(d)). The localized mode is excited by resonating surface plasmons at the sidewalls of the metal structure (vertical SPPs, also called gap or cavity modes[24,47]). Vertical SPPs have been the subject of extensive studies mainly linked to the EOT effect described by Ebbesen *et al.* in 2D hole arrays.[1] It is worth noting that in one dimensional gratings, different transmission mechanisms can occur and *e.g.* no coupling between the SPP modes on the top and bottom surfaces is required.[48,49] In contrast to the majority of research in this area, our structure is aimed at creating a strong response in reflection instead of transmission, which is especially advantageous for visual applications under ambient lighting or remote readout.

Transverse magnetic (TM) polarized reflection spectra of the fabricated aluminum nanowires reveal a pronounced Fano-resonance, which is red-shifted and more damped for gold (90 nm of metal evaporated at $\alpha = 56°$, dashed lines in Fig. 1(e) and (f)). When we compare these spectra to computations (solid lines) performed on the model from Fig. 1(d) with parameters deduced from the SEM image, we observe very good spectral alignment of the maxima and minima for both materials. The fabricated aluminum structure also shows a very strong spectral modulation, whereas the resonance is attenuated and broadened for the gold wires. This can most likely be linked to the increased absorption of gold at visible wavelengths, which is amplified by the presence of fabrication imperfections. Imperfections and absorption reduce in turn the modulation of the Fano-resonance and broaden the features. Because of this attenuation, the WR anomaly around λ = 525 nm is also more visible in the measurement than in the simulation, where it only appears as a shoulder.[10] Due to the thermal evaporation process, both materials can also suffer from altered optical properties when compared to bulk values found in the literature; the corresponding defects (*e.g.* granularity and roughness) could be possibly improved.[50] It is also clear that the resonators resulting from this replication based process are not as well defined as *e.g.* metal nanostructures resulting from electron beam lithography and show rounded shapes. The resulting lowered efficiencies and broader features are however typical observations when considering industrial fabrication of nanostructures.

In order to explain the involved modes, we start with gold, which is the most explored plasmonic material and particularly popular for biosensing applications. Fig. 2 shows the far-field properties of such U-shaped nanowires, together with near-fields and charge maps at specific spectral positions. The short wavelength end of the observed Fano-resonance (position 1, around λ = 600 nm) is in the vicinity of the WR anomaly, whose spectral position is determined by $\lambda = (n_2 - n_1 \sin\theta_i)\Lambda/m$, where n_1 is the refractive index of the incident medium, n_2 is the refractive index of the substrate, θ_i is the incident angle of the irradiated light, Λ is the grating period and m is the diffraction order. For the vanishing first order in our Λ = 350 nm grating, we have $n_1 = n_2 = 1.5$, $\Theta_i = 0$ and $m = 1$ and we obtain λ = 525 nm (the refractive index of substrate and superstrate are identical). Hence, the near-field at position 1 shows no higher order diffraction and is dominated by the propagating SPP excited on the incident side of the structure as evidenced by the near-field. The electric field inside the cavity

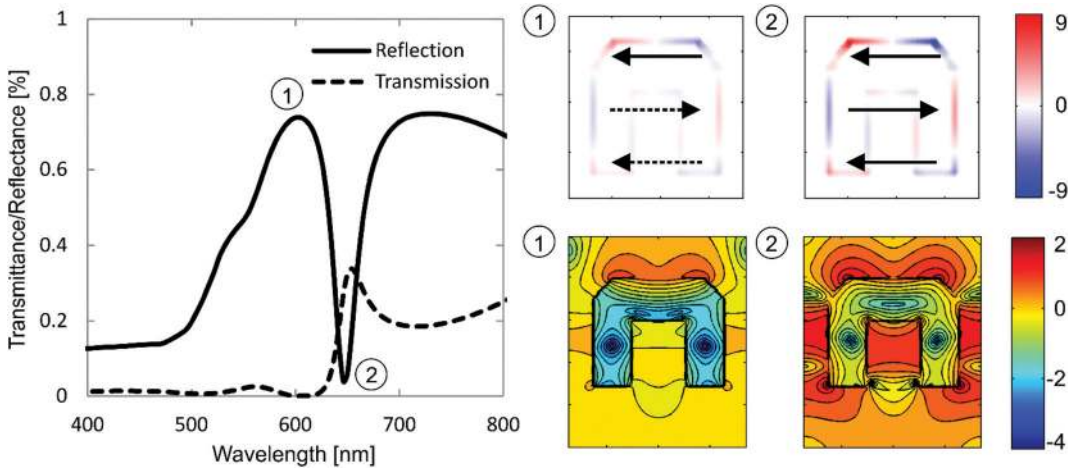

Fig. 2 Simulations of the reflected (solid line) and transmitted (dashed line) far-field (left) have been performed with the surface integral equation method (SIE) and are shown together with the computed charge distributions (top right) and near-fields (bottom right) at selected spectral positions for 90 nm gold evaporated at each side of the grating (350 nm period, 200 nm depth, w = 0.3).

is very low and long lobes with a high field intensity extend towards the incident direction of the light, which is the signature of a propagating SPP mode at the surface of the grating. Strong charges are also present on the top part of the wire, forming a radiating dipole in each structure.

This results in a high reflectivity, which is a well-known feature of metallic gratings for wavelengths close to the WR anomaly.[51,52] At the reflectance minimum of the Fano-resonance (position 2, around λ = 650 nm), the near-field shows similar lobes on the top surface, indicating the continued presence of the horizontal SPP. In contrast to position 1, additional field maxima exist now at the cavity center and its far end, which are likely caused by vertical SPP modes (no SPP is visible on the back side). This coupled mode has the highest field enhancement of all the spectral positions and exhibits a hexapolar distribution of charges in the structure. Absorbance is maximal at position 2 (besides wavelengths below 550 nm, where gold intrinsically absorbs), which is a typical feature of subradiant modes.

Towards the infrared region of the Fano-resonance, the horizontal SPP vanishes gradually. The complete infrared portion of the spectrum, where quadrupolar and dipolar localized plasmon modes (2nd and 1st order modes) are observed, is available in the ESI.†

Switching from gold to aluminum allows plasmonic resonances to access the green, blue and even ultraviolet wavelengths, which makes it a much better choice for visual applications. Changing to aluminum also causes all the plasmonic modes to shift towards lower wavelengths (by around 70 nm, compare Fig. 1(e) and (f)) since the excitation of plasmonic resonances requires a higher energy in aluminum. As a result, the Fano-resonance is moved further towards the WR anomaly since the position of the WR anomaly only depends on the grating parameters and is independent of the plasma frequency of the metal. At wavelengths below the WR anomaly, a part of the incident light is redistributed into higher diffraction orders, which in turn leads to lower specular reflectance. A feature of this spectral proximity of the Fano-resonance to the WR anomaly is therefore a significant lowering of the peak's full width at half maximum. Choosing the period such that the WR anomaly lies at the lower wavelength end of the Fano-resonance is a straight-forward way to take advantage of such spectral features. They are especially favorable for sensing since a small spectral shift of the peak leads to a strong intensity response at the initial peak wavelength.

On the other hand, the comprehension of the modes becomes more complicated when the evaporated material is aluminum and the plasmonic resonances overlap with the WR anomaly (Fig. 3). Yet, we can use the different observations made for gold although the hexapolar charge distribution cannot be found at the resonance minimum (position 3) but is

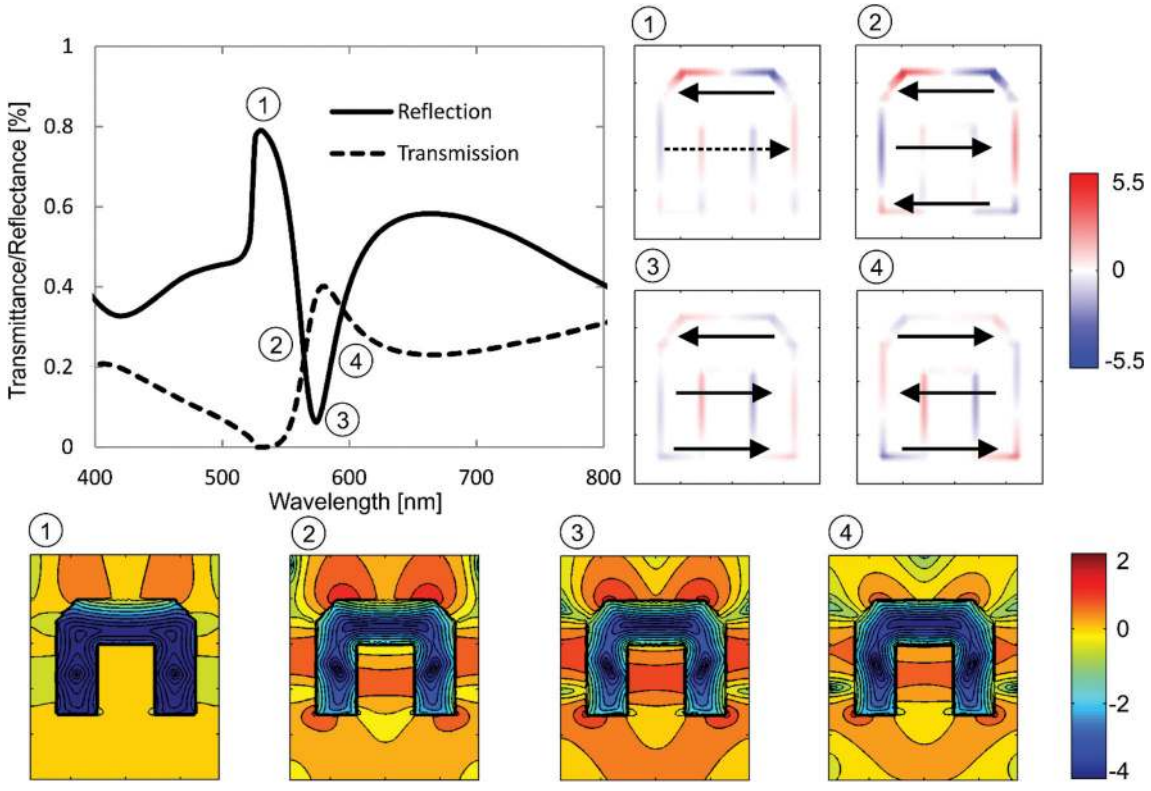

Fig. 3 SIE simulations of the reflected (solid line) and transmitted (dashed line) far-fields (top left) are shown together with the computed charge distributions (top right) and near-fields (bottom) at selected spectral positions for 90 nm aluminum evaporated at each side of the grating (350 nm period, 200 nm depth, w = 0.3).

shifted to the short wavelength slope (position 2). Besides the diminishing horizontal SPP (long lobes at the incident interface become flatter with increasing wavelength), no significant near-field variations are visible when comparing the three positions around the resonance minimum.

In contrast, the charge distribution is substantially altered: the hexapole found at position 2 first experiences a switch of the charge distribution at the bottom end of the sidewalls (position 3) before all of the charges appear inverted when looking at the long wavelength slope of the resonance (position 4). Similar phenomena have been observed close to Fano-resonances in other systems[12,53] and can be related to a classical oscillator driven off-resonance: if the input frequency is low, the resonator will oscillate in phase with the incoming field but for frequencies above the resonance frequency of the oscillator, they will be 180° out of phase. It is worth mentioning that charges are only rarely simulated in metallic gratings. As presented above, they can provide valuable insights into the nature of the resonance at hand and the exact mode of interaction between the incident field and the resonator. In the present Al grating we see for example that the hexapolar mode is attenuated and switches sign at the minimum, which influences the sensitivity of the resonator towards its surrounding. The investigation of charges can therefore contribute greatly to the understanding of plasmonic systems and help tailoring them for specific needs.

At increasing angles of incidence θ in classical grating mount (angle between incident light and surface normal; the plane of incidence is perpendicular to the grating lines), the WR anomaly and the propagating SPP redshift and lead to the disappearance of the Fano-resonance (Fig. 4(a), 155 nm). On the other hand, a reflectance peak remains around λ = 600 nm at high incidence angles, corresponding to the localized hexapolar mode. For this incidence angle, the resonance is decoupled from the SPP and its original dispersion can be retrieved. Another way of tuning the resonance away from the WR anomaly is by increasing the sidewall length. Fig. S4(c)† verifies the preservation of the hexapolar charge distribution in the case of h = 450 nm (Fig. 4(h)) at a wavelength of 1325 nm in absence of the horizontal SPP (no lobes in the near-field, Fig. S4(b)†). In general, the angle dependence of the resonance strongly decreases as it is decoupled from the SPP (indicated by the purple line in Fig. 4(a)–(d) for the aluminum case, which serves as a guide to the eye). This is intuitive as – in contrast to thin film interference, where the resonating wavelength depends on the angle of incidence – the present

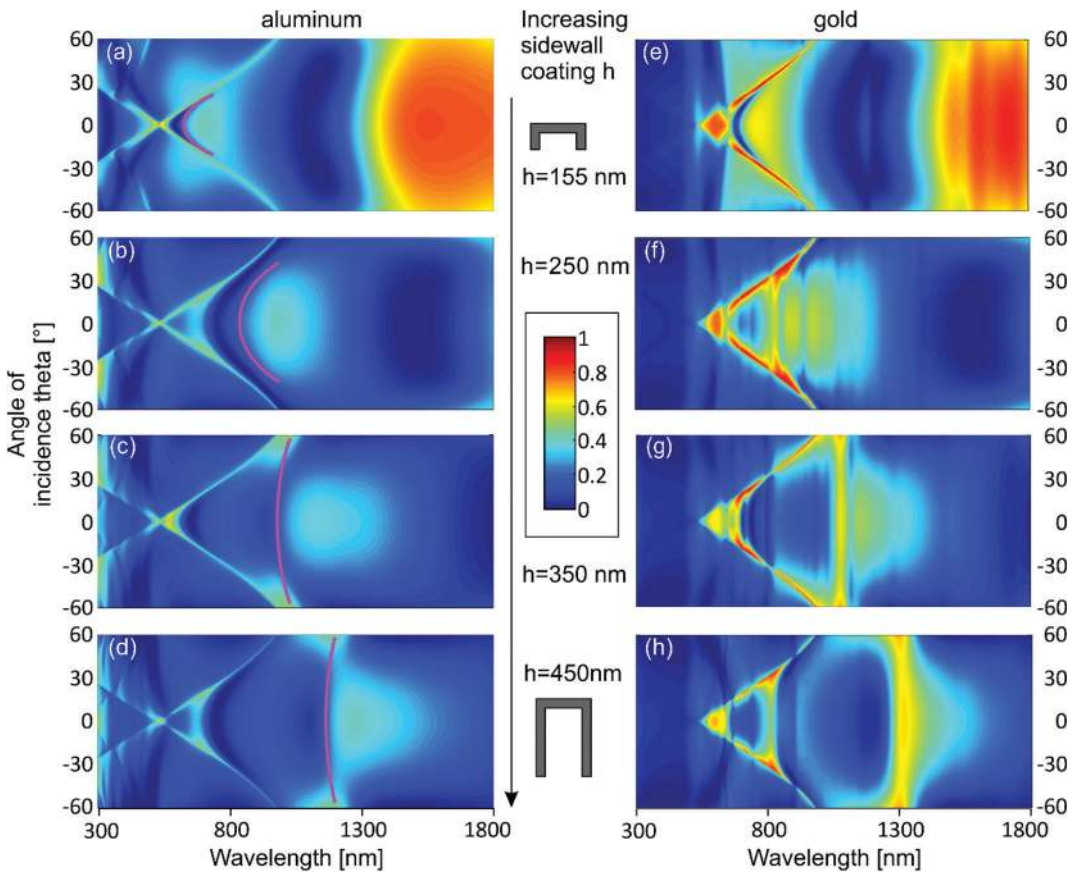

Fig. 4 Computed reflectances (intensities in color map) are shown for wavelengths between 300 nm and 1800 nm and angles of incidence from −60° to 60° (inside the medium). The sidewall length is varied between (a) h = 155 nm and (d) h = 450 nm in aluminum (left) as well as gold wires (right, (e) h = 155 nm and (h) h = 450 nm).

resonance is confined to the wires. Hence, the shape of the wires and their spacing are the main determinant parameters for the resonance position. The angle of incidence on the other hand determines how strong the incident field can couple to this resonance (weaker coupling at increasing angles of incidence is especially visible for aluminum in the form of darker blue colors in Fig. 4). The retrieval of this undisturbed dispersion confirms the proposed localized mode since similar observations were reported earlier.[28,48] Also, the sharp, destructive Fano-like interference coming from the SPP is alleviated and the lineshape turns into a broader, less asymmetric resonance (see ESI, Fig. S4†). The increased width of the resonance is amplified by the red-shift, which leads to an enhancement of the radiative losses.[12,54] We would like to point out that also the spectral width of the dip is much narrower when it is in the proximity of the WR anomaly. This beneficial effect has been observed earlier and can be attributed to strong coupling between the SPP and the LSPR.

In summary, we have shown that the present resonance constitutes of two plasmonic modes, a hexapolar, localized plasmonic mode and a SPP on the incident, flat side of the U-shape. The localized plasmon shows a broad lineshape whose spectral position depends on the height of the sidewalls.[48] When it couples to the SPP, a typical, asymmetric Fano-resonance is observed. The destructive interference from the Wood-Rayleigh anomaly finally further enhances the resonance modulation.

As a side note it is worth mentioning that, in the present example, the groove on the back side of the structure (introduced by the initial dielectric grating) mainly leads to enhanced transmittance when compared to solid metal wires (see ESI, Fig. S3†). A minor shift of the quadrupolar mode

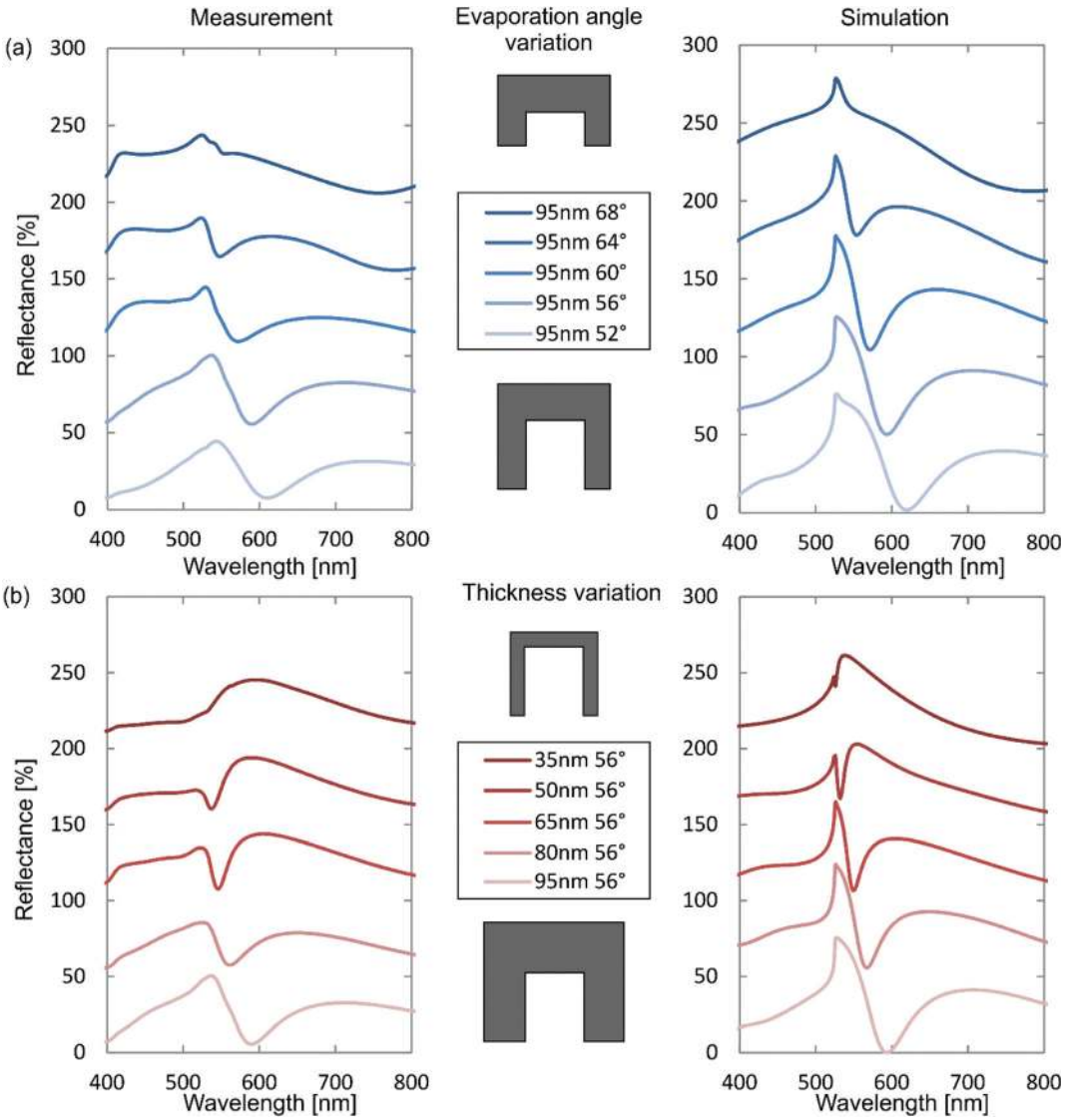

Fig. 5 Measured (left) and computed (right) spectra for (a) Al structures evaporated with different angles (blue) and (b) thicknesses (red). The curves are shifted by 50%.

could also be observed (Fig. S3,† minimum around λ = 1000 nm). Research on similar structures however showed that strongly enhanced absorption may result from the introduction of grooves.[27,29] Fully exploring this effect would go beyond the scope of this article, but proper tuning of the parameters also led to very high absorbance values (above 95%) in our simulations.

Since the resonance wavelength of the hexapole depends on the sidewall height h, it is possible to tune its spectral position by adjusting the evaporation angle. The steeper the angle α is, the shorter the coatings on the grating sidewalls become, hence leading to shorter U-shapes after encapsulation. Fig. 5 (a) shows how such an adjustment of α affects the spectrum: the maximum caused by the WR anomaly stays at around λ = 525 nm as expected, since it only depends on the grating period and not the wire parameters. On the other hand, the minimum can be shifted from around λ = 550 nm for α = 64° to above λ = 600 nm for α = 52°. If the evaporation angle becomes too flat, the minimum shifts into the WR anomaly and vanishes.

The shape of the resonance can also be tuned by changing the thickness of the evaporated metal (Fig. 5(b)). First, increasing the evaporated metal thickness increases the height of the wires due to the additional material deposited on the grating ridge. It is therefore not surprising that the hexapolar mode shifts towards longer wavelengths for a thicker metallization. In addition to this effect, tuning the metal thickness allows controlling the height of the reflection maximum close to the WR anomaly. It is clearly visible that the peak is strongly attenuated for a thinner metallization. When considering that SPPs on the top surface of the structure are an important constituent of this feature (no SPPs can be excited on the back side due to the sidewalls[25]), we can relate our structure to plasmonic waveguides: short-range SPPs, which are comparable to the present SPPs, can experience stronger confinement and hence higher losses when propagating on thinner metal films.[55] In our case, we expect this mechanism to increase the non-radiative losses in a stronger way than the radiative ones and hence an attenuated reflectance peak is observed.

Both parameters are readily adjustable in lab-scale evaporators, but also in a roll-to-roll production line these adjustments can be done on the fly. Usually, the embossed structure needs to be adapted in order to shift the resonance, which requires exchanging the embossing master. For such an exchange, the machine of course needs to be halted. Since this is not necessary with the proposed technique, the added flexibility is very valuable for industrial production if the device's reflectance is for instance monitored in-line. Measurements and simulations with rigorous coupled wave analysis (RCWA[56]) show good agreement for all the cases investigated in this work (left and right column in Fig. 5). The RCWA method allows significant reduction of the computation time when compared to surface integral equation method, which is essential when screening through suitable parameters for production. It is worth noting that for thicker metal layers or flatter angles α, the shape of the metal structures can change significantly and the use of more sophisticated models might become necessary.

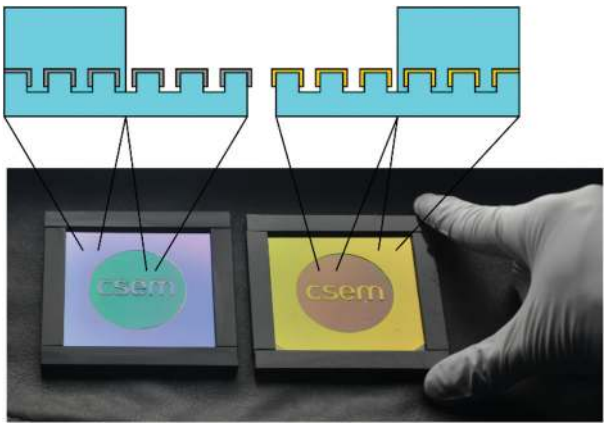

Fig. 6 Photograph of aluminum (left) and gold (right) evaporated samples sharing the same parameters otherwise. The image also shows the contrast between embedded (border and letters) and air interfaced parts (circular area) of the structure, when viewed through a polarizer.

The choice of materials is a final way of tuning the resonance. The difference between structures fabricated with either of the two metals is even evident to the naked eye as illustrated by the photo (taken through a polarizer oriented perpendicular to the grating lines) in Fig. 6: the embedded aluminum wires (left) show a strong purple color at an angle of view of around 45°, whereas the gold evaporated grating (right) is yellow. A strong contrast is also visible between encapsulated regions of the samples (letters and border) and the areas interfacing air (central round shape, compare with sketches). Strong spectral responses are therefore also expected for polymer coatings with different refractive indices or refractive index changes in a sensing layer. This motivates the use of the reported structure for optical sensing on large surfaces (maybe even for visual read-out like *e.g.* demonstrated for protein monolayers by Yanik *et al.*[14]) or structural colors, which can handily be controlled by properly choosing the polymer coating.

3 Experimental

3.1 Simulations

The simulation model for RCWA calculations is shown in Fig. 1(d). The refractive index of the surrounding medium (incident as well as substrate) was assumed to be 1.5, data for aluminum were taken from Rakic *et al.*[57] and the optical constants for gold were adapted from Johnson and Christy.[58]

The geometrical parameters are: Λ = 350 nm and w = 0.3 Λ. The thickness of the evaporated Al was measured on the sample and used as an estimate for t (reduced by 5–10 nm due to the native oxide layer). The thickness on the sidewalls can be calculated by $s = t\tan(\alpha)$ (geometrical considerations).

From the thickness as set on the evaporator (D), t can also be calculated with $t = \cos(\alpha)D$. For the height of the sidewall

coating h, an approximate value can be obtained with $h = \tan(\alpha)(\Lambda - w)$. One has to keep in mind that this value is quite accurate for the evaporation from the first side, but during the second evaporation, the already deposited metal will increase the shadowing effect and therefore cause h to be shorter on this side. This effect was accounted for by decreasing h compared to the above calculation by 5–15 nm (depending of the metallization thickness) but keeping the structure symmetric for simplicity. The SEM image in Fig. 1(c) finally also shows rounded corners, which inspired the missing corner pieces of width $s/2$ and height $t/2$ for our RCWA simulations.

The model for surface integral equation (SIE) simulations contained slanted facets instead of the missing corner piece, which is a more accurate representation of reality but not available with RCWA (which requires layered media as an input). The simulations are in close agreement for both methods.

3.2 Fabrication and characterization

Holographically originated binary gratings (350 nm period and 200 nm depth with $w = 0.3$) have been electroplated and subsequently used for nanoimprinting with the UV curable resin Ormocomp® (Micro Resist Technology GmbH) on 3 inch edge length, square glasses. The casts were baked over night at 165 °C. The gratings were then evaporated at an angle between $\alpha = 52°$ and $\alpha = 68°$ with respect to the surface normal from both sides (perpendicular to the grating lines) in a BAK 550 (Oerlikon Balzers). The evaporated material thickness as set on the machine was varied between $D = 35$ nm and $D = 95$ nm for each side (this is the value referred to throughout the article). Accuracy of the parameter was verified with a KLA Tencor P-10 profilometer on a flat part of the sample. This value was then also used for building the model for simulations, keeping in mind that, for oblique deposition, only a fraction of the evaporated amount of material actually reaches the sample (proportional to $\cos(\alpha)$).

For SEM measurements, the sample was cleaved perpendicular to the grating lines, sputtered with 10 nm of gold and subsequently imaged in a Hitachi S-4100. Note that breaking the sample for SEM can deform the metal structures and lead to defects at the edge. The presented images therefore tend to overestimate roughness and irregularities.

The nanostructures were covered with Ormocomp® and finally measured in a Lambda 9 spectrophotometer (Perkin Elmer Inc.) with TM polarized illumination (see Fig. 1).

4 Conclusions

We have presented an industry compatible way of fabricating Fano-resonant aluminum and gold nanostructures on large surfaces. We could avoid serial patterning like e-beam lithography by using holographically produced gratings together with oblique metal deposition. By means of far-field as well as near-field and charge calculations, the subradiant mode of the Fano-resonance was determined to be a surface plasmon polariton coupled to a localized plasmon mode. The coupled mode exhibits a hexapolar charge distribution, associated with high electric near-fields and a strongly enhanced absorbance. We were able to tune the resonance position and spectral intensity distribution through the change of easily accessible evaporation parameters. This property makes our structure very attractive for high-throughput, low-cost production such as roll-to-roll manufacturing. Finally, the steep Fano-lineshape of our structure is appealing for incorporation into sensors, which can be applied to large areas and provide an optical response directly visible to the naked eye. The design of different physical colors through proper choice of the polymer coating is another promising path to investigate.

Acknowledgements

The authors would like to acknowledge Daniele Casari for his support in fabricating the presented nanostructures and Dr Martin Stalder for the inspiring discussions. Funding from CCMX-Fanosense is also gratefully acknowledged.

Notes and references

1 T. W. Ebbesen, H. J. Lezec, H. F. Ghaemi, T. Thio and P. A. Wolff, *Nature*, 1998, **391**, 667–669.
2 K. A. Willets and R. P. Van Duyne, in *Annual Review of Physical Chemistry*, Annual Reviews, Palo Alto, 2007, vol. 58, pp. 267–297.
3 J. Butet and O. J. F. Martin, *ACS Nano*, 2014, **8**, 4931–4939.
4 T. Maurer, J. Marae-Djouda, U. Cataldi, A. Gontier, G. Montay, Y. Madi, B. Panicaud, D. Macias, P.-M. Adam, G. Lévêque, T. Bürgi and R. Caputo, *Front. Mater. Sci.*, 2015, **9**, 170–177.
5 H. A. Atwater and A. Polman, *Nat. Mater.*, 2010, **9**, 205–213.
6 J. Sauvage-Vincent, Y. Jourlin, S. Tonchev, C. Veillas, P. Claude and O. Parriaux, *Proc. SPIE*, 2012, **8428**, 84280F.
7 X. M. Goh, Y. Zheng, S. J. Tan, L. Zhang, K. Kumar, C.-W. Qiu and J. K. W. Yang, *Nat. Commun.*, 2014, **5**, 5361.
8 S. J. Tan, L. Zhang, D. Zhu, X. M. Goh, Y. M. Wang, K. Kumar, C.-W. Qiu and J. K. W. Yang, *Nano Lett.*, 2014, **14**, 4023–4029.
9 K. Kumar, H. Duan, R. S. Hegde, S. C. W. Koh, J. N. Wei and J. K. W. Yang, *Nat. Nanotechnol.*, 2012, **7**, 557–561.
10 B. Luk'yanchuk, N. I. Zheludev, S. A. Maier, N. J. Halas, P. Nordlander, H. Giessen and C. T. Chong, *Nat. Mater.*, 2010, **9**, 707–715.
11 B. Gallinet and O. J. F. Martin, *ACS Nano*, 2011, **5**, 8999–9008.
12 A. Lovera, B. Gallinet, P. Nordlander and O. J. F. Martin, *ACS Nano*, 2013, **7**, 4527–4536.
13 A. Christ, G. Lévêque, H. Fischer, A. Nesci, S. G. Tikhodeev and O. J. F. Martin, in Optical MEMS and Their Applications Conference, 2006. IEEE/LEOS International Conference on, IEEE, 2006, pp. 66–67.

14 A. A. Yanik, A. E. Cetin, M. Huang, A. Artar, S. H. Mousavi, A. Khanikaev, J. H. Connor, G. Shvets and H. Altug, *Proc. Natl. Acad. Sci. U. S. A.*, 2011, **108**, 11784–11789.
15 A. E. Miroshnichenko, S. Flach and Y. S. Kivshar, *Rev. Mod. Phys.*, 2010, **82**, 2257–2298.
16 V. A. Fedotov, M. Rose, S. L. Prosvirnin, N. Papasimakis and N. I. Zheludev, *Phys. Rev. Lett.*, 2007, **99**, 147401.
17 J. Zhao, C. Zhang, P. V. Braun and H. Giessen, *Adv. Mater.*, 2012, **24**, OP247–OP252.
18 N. Verellen, Y. Sonnefraud, H. Sobhani, F. Hao, V. V. Moshchalkov, P. V. Dorpe, P. Nordlander and S. A. Maier, *Nano Lett.*, 2009, **9**, 1663–1667.
19 M. Rahmani, B. Luk'yanchuk and M. Hong, *Laser Photonics Rev.*, 2013, **7**, 329–349.
20 A. Christ, G. Lévêque, O. J. F. Martin, T. Zentgraf, J. Kuhl, C. Bauer, H. Giessen and S. G. Tikhodeev, *J. Microsc.*, 2008, **229**, 344–353.
21 B. Gallinet, L. Davoine, G. Basset and M. Schnieper, *Proc. SPIE*, 2013, **8818**, 88180Z.
22 Y.-L. Ho, A. Portela, Y. Lee, E. Maeda, H. Tabata and J.-J. Delaunay, *Adv. Opt. Mater.*, 2014, **2**, 522–528.
23 S.-W. Ahn, K.-D. Lee, J.-S. Kim, S. H. Kim, J.-D. Park, S.-H. Lee and P.-W. Yoon, *Nanotechnology*, 2005, **16**, 1874–1877.
24 T. Siegfried, Y. Ekinci, O. J. F. Martin and H. Sigg, *Nano Lett.*, 2013, **13**, 5449–5453.
25 A. Barbara, P. Quémerais, E. Bustarret and T. Lopez-Rios, *Phys. Rev. B: Condens. Matter*, 2002, **66**, 161403(R).
26 B. Gallinet, T. Siegfried, H. Sigg, P. Nordlander and O. J. F. Martin, *Nano Lett.*, 2013, **13**, 497–503.
27 H. Gao, C. Gu, Z. Y. Zheng, S. J. Chen and H. Y. Hao, *Appl. Phys. B*, 2014, 1–9.
28 V. I. Belotelov, A. N. Kalish, A. K. Zvezdin, A. V. Gopal and A. S. Vengurlekar, *J. Opt. Soc. Am. B*, 2012, **29**, 294–299.
29 H.-Q. Li, K.-J. Wang, Z.-G. Yang and J.-S. Liu, *J. Opt. Soc. Am. B*, 2014, **31**, 806–809.
30 S. Collin, F. Pardo, R. Teissier and J.-L. Pelouard, *J. Opt. A: Pure Appl. Opt.*, 2002, **4**, S154.
31 A. Feuerstein and M. Mayr, *IEEE Trans. Magn.*, 1984, **20**, 51–56.
32 S. H. Ahn and L. J. Guo, *Adv. Mater.*, 2008, **20**, 2044–2049.
33 S. Cataldo, J. Zhao, F. Neubrech, B. Frank, C. Zhang, P. V. Braun and H. Giessen, *ACS Nano*, 2012, **6**, 979–985.
34 T. Siegfried, Y. Ekinci, H. H. Solak, O. J. F. Martin and H. Sigg, *Appl. Phys. Lett.*, 2011, **99**, 263302.
35 D. Gérard and S. K. Gray, *J. Phys. D: Appl. Phys.*, 2015, **48**, 184001.
36 G. V. Naik, V. M. Shalaev and A. Boltasseva, *Adv. Mater.*, 2013, **25**, 3264–3294.
37 M. W. Knight, N. S. King, L. Liu, H. O. Everitt, P. Nordlander and N. J. Halas, *ACS Nano*, 2013, **8**, 834–840.
38 C. Langhammer, M. Schwind, B. Kasemo and I. Zorić, *Nano Lett.*, 2008, **8**, 1461–1471.
39 Lawrence Livermore National Laboratory.
40 M. T. Gale, M. Rossi, H. Schütz, P. Ehbets, H. P. Herzig and D. Prongué, *Appl. Opt.*, 1993, **32**, 2526.
41 L. Peng, Y. Deng, P. Yi and X. Lai, *J. Micromech. Microeng.*, 2014, **24**, 013001.
42 P. Nussbaum, I. Philipoussis, A. Husser and H. P. Herzig, *Opt. Eng.*, 1998, **37**, 1804–1808.
43 L. Yu, C. G. Koh, L. J. Lee, K. W. Koelling and M. J. Madou, *Polym. Eng. Sci.*, 2002, **42**, 871–888.
44 M. Matschuk and N. B. Larsen, *J. Micromech. Microeng.*, 2013, **23**, 025003.
45 S. Traut and H. P. Herzig, *Opt. Eng.*, 2000, **39**, 290–298.
46 N. C. Lindquist, P. Nagpal, K. M. McPeak, D. J. Norris and S.-H. Oh, *Rep. Prog. Phys.*, 2012, **75**, 036501.
47 D. Crouse and P. Keshavareddy, *Opt. Express*, 2005, **13**, 7760–7771.
48 J. A. Porto, F. J. Garcia-Vidal and J. B. Pendry, *Phys. Rev. Lett.*, 1999, **83**, 2845–2848.
49 F. J. Garcia-Vidal, L. Martin-Moreno, T. W. Ebbesen and L. Kuipers, *Rev. Mod. Phys.*, 2010, **82**, 729–787.
50 K. M. McPeak, S. V. Jayanti, S. J. P. Kress, S. Meyer, S. Iotti, A. Rossinelli and D. J. Norris, *ACS Photonics*, 2015, **2**, 326–333.
51 A. Roszkiewicz and W. Nasalski, *J. Phys. B: At., Mol. Opt. Phys.*, 2013, **46**, 025401.
52 Y. Jourlin, S. Tonchev, A. V. Tishchenko and O. Parriaux, *IEEE Photonics J.*, 2014, **6**, 1–6.
53 R. Verre, Z. J. Yang, T. Shegai and M. Käll, *Nano Lett.*, 2015, **15**, 1952–1958.
54 M. A. Kats, N. Yu, P. Genevet, Z. Gaburro and F. Capasso, *Opt. Express*, 2011, **19**, 21748–21753.
55 D. K. Gramotnev and S. I. Bozhevolnyi, *Nat. Photonics*, 2010, **4**, 83–91.
56 M. G. Moharam and T. K. Gaylord, *J. Opt. Soc. Am.*, 1981, **71**, 811.
57 A. Rakic, *Appl. Opt.*, 1995, **34**, 4755–4767.
58 P. B. Johnson and R. W. Christy, *Phys. Rev. B: Solid State*, 1972, **6**, 4370–4379.

Electronic Supplementary Material (ESI) for Nanoscale.

Supporting Information

Fano-Resonant Aluminum and Gold Nanostructures Created with a Tunable, Up-Scalable Process

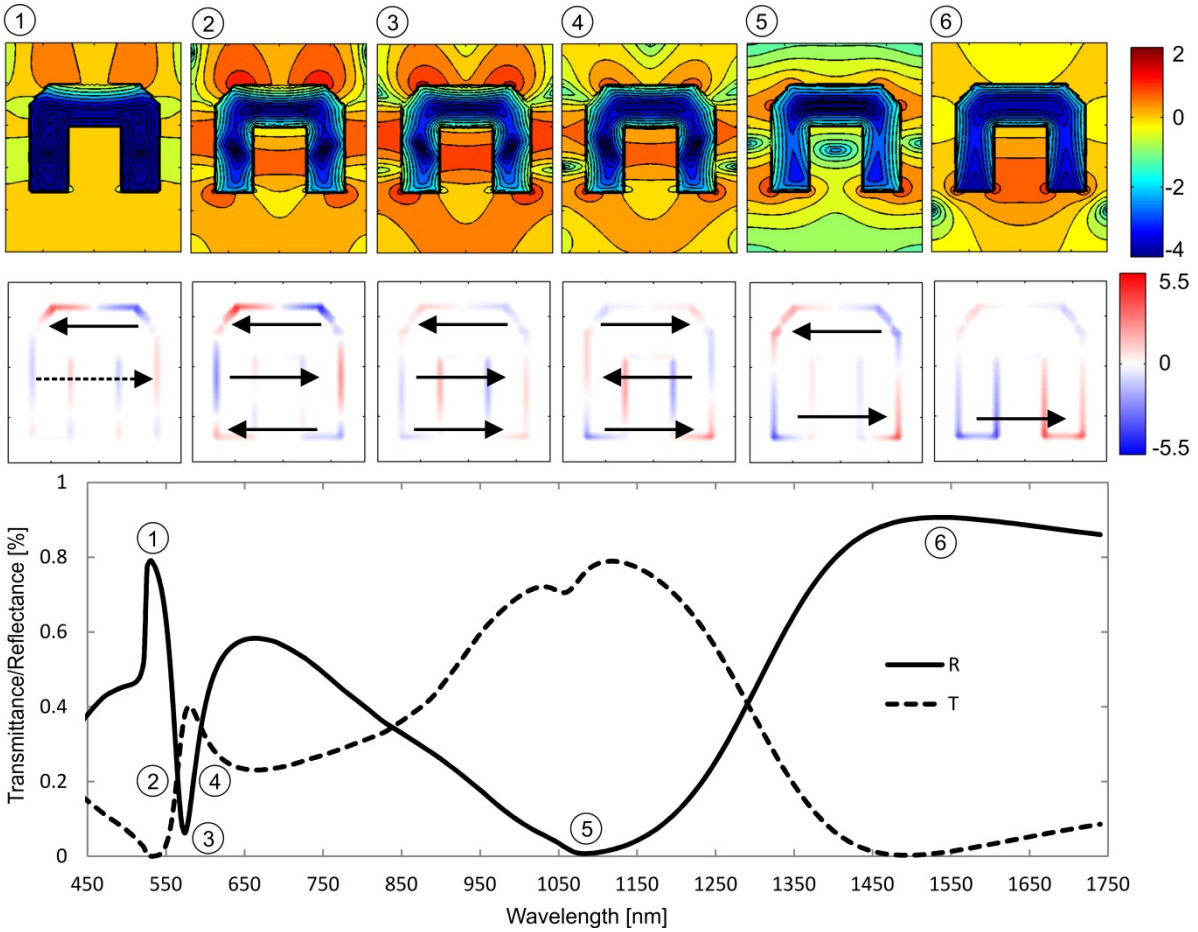

Figure S1: SIE simulations of the reflected (solid line) and transmitted (dashed line) far-fields (bottom) are shown together with the computed near-fields (top) and charge distributions (middle) at selected spectral positions for 90 nm aluminum evaporated at each side of the grating.

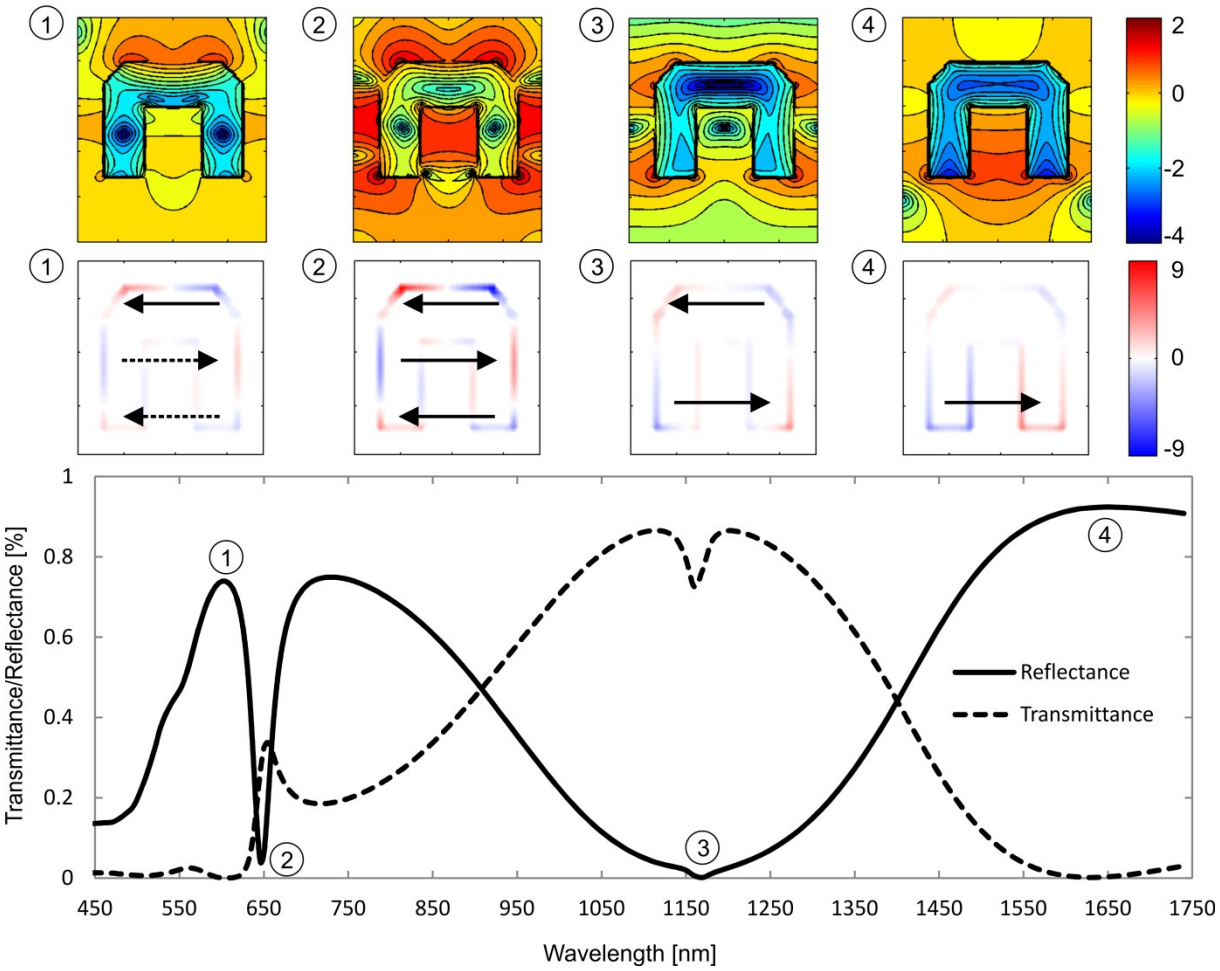

Figure S2: SIE simulations of the reflected (solid line) and transmitted (dashed line) far-fields (bottom) are shown together with the computed near-fields (top) and charge distributions (middle) at selected spectral positions for 90 nm gold evaporated at each side of the grating.

Positions 3 (at λ = 1170 nm) and 4 (λ = 1650 nm) in Figure S2 correspond to the lower order plasmonic modes, with two maxima and a single maximum between the structures respectively. A quadrupole with enhanced absorbance is formed at Position 3 and a radiative dipole is visible at Position 4. The charges are weaker for theses modes, which accounts for the decreased losses (absorbance) when compared to the hexapolar mode.

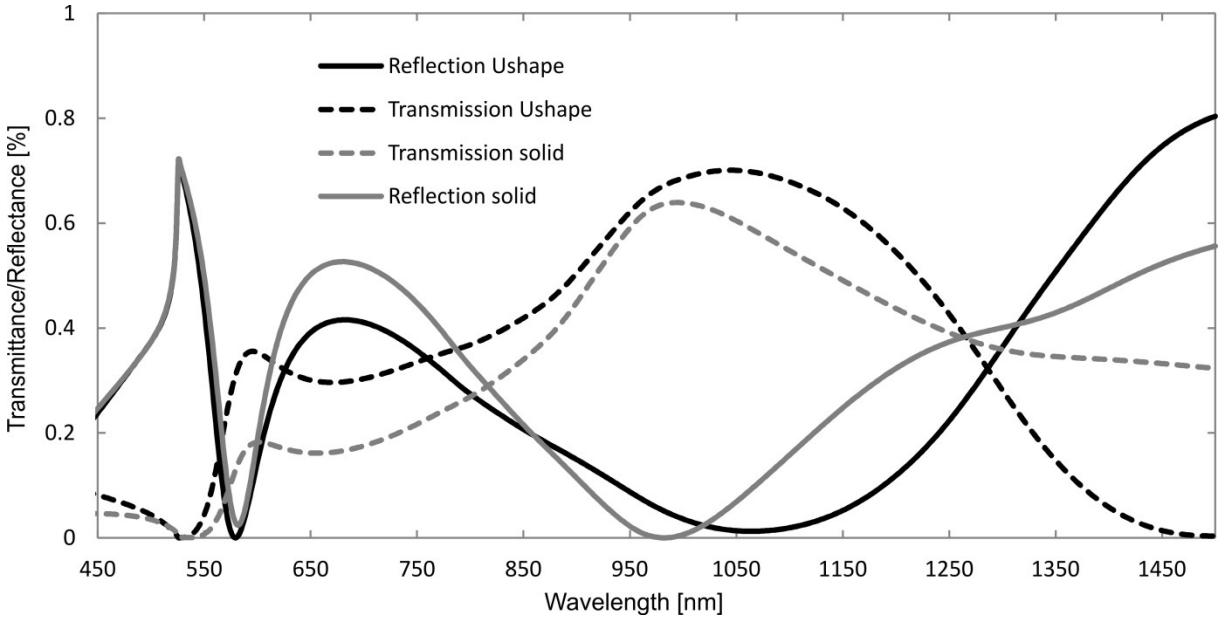

Figure S3: Comparison of the optical properties of U-shaped wires and solid aluminum wires (missing the backside groove)

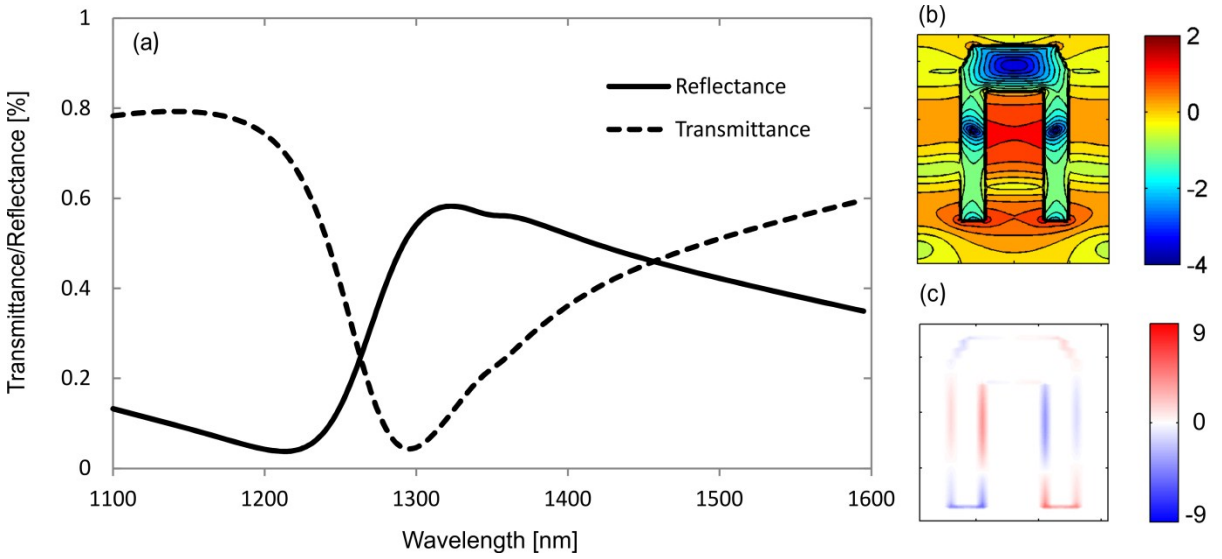

Figure S4: A Part of the spectrum for the 450 nm deep gold structure from Figure 4 is shown (a) together with the near-field (b) and charge distribution (c) at the reflectance maximum.